MITSUBISHI ELECTRIC RESEARCH LABORATORIES
http://www.merl.com

Modeling of transient characteristics of an air source heat pump with vapor injection during reverse-cycle defrosting

Qiao, H.; Aute, V.; Radermacher, R.

TR2018-066 July 12, 2018

Abstract

A thorough literature review indicates that there is a dearth of modeling studies on the defrosting dynamics of air source heat pumps (ASHPs) due to the complex underlying physics and numerous computation details. In an effort to bridge the research gap, this paper first presents a five-stage hot-gas defrost model which is incorporated into a distributed-parameter heat exchange model integrated with a detailed frost growth model proposed in Qiao et al. (2017). Numerical treatments are then proposed to smooth the discontinuous transition between different defrosting stages, resulting in a significant improvement in numerical robustness. The developed models and the component models described in Qiao et al. (2015a) are applied to construct the system model of an air source flash tank vapor injection (FTVI) heat pump. A dynamic simulation is conducted to explore the transient fluid flow and heat transfer phenomena of the system during the reverse-cycle defrosting (RCD). A detailed description of the resulting physical processes is provided. The simulation results indicate that the energy used to melt the frost accounts for 17.7% of the total energy supply from the refrigerant flow, which is consistent with published experimental data for the efficiency of a typical defrosting process.

Applied Energy

Modeling of transient characteristics of an air source heat pump with vapor injection during reverse-cycle defrosting

Hongtao Qiao[a,*], Vikrant Aute[b], Reinhard Radermacher[b]

[a]*Mitsubishi Electric Research Laboratories, 201 Broadway, Cambridge, MA 02139, USA*

[b]*Center for Environmental Energy Engineering, University of Maryland, College Park, 4164 Glenn L. Martin Hall Bldg., MD 20742, USA*

*: Corresponding Author, Tel: +1 (617) 621-7586, E-mail: qiao@merl.com

ABSTRACT

A thorough literature review indicates that there is a dearth of modeling studies on the defrosting dynamics of air source heat pumps (ASHPs) due to the complex underlying physics and numerous computation details. In an effort to bridge the research gap, this paper first presents a five-stage hot-gas defrost model which is incorporated into a distributed-parameter heat exchange model integrated with a detailed frost growth model proposed in Qiao *et al*. (2017). Numerical treatments are then proposed to smooth the discontinuous transition between different defrosting stages, resulting in a significant improvement in numerical robustness. The developed models and the component models described in Qiao *et al*. (2015a) are applied to construct the system model of an air source flash tank vapor injection (FTVI) heat pump. A dynamic simulation is conducted to explore the transient fluid flow and heat transfer phenomena of the system during the reverse-cycle defrosting (RCD). A detailed description of the resulting physical processes is provided. The simulation results indicate that the energy used to melt the frost accounts for 17.7% of the total energy supply from the refrigerant flow, which is consistent with published experimental data for the efficiency of a typical defrosting process.

Keywords: Modeling; Frosting; Defrosting; Dynamic characteristics; Vapor injection; Heat pump

NOMENCLATURE

Symbols

A	area [m^2]
c_p	specific heat [J kg^{-1} K^{-1}]
c_{sv}	vaporization coefficient of surface water [m s^{-1}]
f	frictional factor [-]
h	specific enthalpy [J kg^{-1}]
k	thermal conductivity [W m^{-1} K^{-1}]
Le	Lewis number [-]
$\dot{m}$	mass flow rate [kg s^{-1}]
p	pressure [N m^{-2}]
t	time [s]
T	temperature [K]

Greek letters

α	heat transfer coefficient [W m^{-2} K^{-1}]
δ	thickness [m]
ε	emissivity [-]
φ	valve opening fraction [-]
ρ	density [kg m^{-3}]
σ	Boltzmann constant [m^2 kg^2 s^{-2} K^{-1}]
τ	time constant [s]
ω	humidity ratio [kg H_2O per kg dry air]

Δ	difference [-]

Subscripts

a	air
amb	ambient
eff	effective
f	frost
face	frontal face of coil surface
fg	liquid to gas
fs	frost surface
H_2O	water
i	internal
ig	ice to gas
in	inlet
max	maximum
min	minimum
o	external
r	refrigerant
s	surface
w	wall

1 Introduction

Air source heat pumps (ASHPs) are widely used for space heating because of their low cost and ease of installation as well as their high potential for energy and emission savings. During operation in the winter, frost can form and accumulate on the outdoor heat exchanger when the heat exchanger surface temperatures are below the dew point of ambient air and the freezing point,

which degrades performance significantly due to augmented thermal resistance and reduced airflow. Consequently, defrosting is required to ensure the efficient operation of the system by removing frost build-up and clearing the heat exchanger surfaces.

Among the various methods of defrosting, reverse-cycle defrosting (RCD) is extensively used due to its higher defrosting efficiency. In the RCD, the heat pump system reverses its components: the evaporator becomes a condenser and the condenser becomes an evaporator. The hot gas discharged by the compressor, originally transported to the indoor heat exchanger in the heating mode, is now pumped into the outdoor heat exchanger to melt the frost. Once the defrost cycle ends, the system will reverse its components again and resume to the heating mode.

Although the concept of RCD is simple, the resulting system dynamics are quite involved due to operating mode switch. Extensive experimental studies were conducted to gain a detailed understanding in physical processes of ASHPs during the RCD (O'Neal *et al*., 1989; O'Neal and Peterson, 1990; O'Neal *et al*., 1991; Payne and O'Neal, 1995; Huang *et al*., 2004; Huang *et al*., 2007; Chen and Guo, 2009). In contrast, there are very few theoretic studies in this aspect due to the complex underlying physics and comprehensive computation details. Krakow *et al*. (1993) presented the first paper in which a simplified analytical model was developed to predict the dynamic characteristics of a refrigeration system during the RCD. Unfortunately, their analysis excluded the stage of the refrigerant pressure equalization resulting from energizing the reversing valve, during which the refrigerant dynamics vary dramatically. Liu *et al*. (2003) performed a dynamic simulation to study the transient behavior of an ASHP during the RCD. A subsequent simulation study was performed based on the same simulation models to compare the defrosting performance of an ASHP with R407C and R22 during defrosting (Liu *et al*., 2008). However, many modeling details were omitted in these two related papers. Information about how to model

the reversing valve, the key component in achieving cycle reversal, and how to switch between heating and cooling modes in the simulation was not provided. Additionally, the time evolution of frost thickness during the defrosting cycle was not given in the results, which raises doubts about the capabilities of their models. More importantly, all these three simulation studies only focused on the dynamics of conventional single-stage ASHPs, and none of the current literature has dealt with more advanced two-stage flash tank vapor injection (FTVI) systems, which exhibit far more complicated dynamics.

Compared to the conventional systems without vapor injection, FTVI systems are operated with lower discharge temperatures and have higher performance in energy efficiency, especially under extremely high and low ambient temperature conditions (Wang *et al*., 2009). We have reported the cycling and frosting dynamics of the FTVI systems (Qiao *et al*., 2015a, 2015b, 2016, 2017), but the defrosting characteristics of such systems have never been studied. As a subsequent study of our previous work, a motivation of this paper is to explore the RCD dynamics of FTVI systems via numerical simulation.

In order to fulfill this objective, a five-stage hot-gas defrost model is developed in this paper. Different from the hot-gas defrost models available in the literature (Sanders, 1974; Krakow *et al*., 1992a; Aljuwayhel, 2006; Dopazo *et al*., 2010), the proposed model will use numerical treatments to smooth the discontinuous transitions between different defrosting stages to improve numerical stability. This defrost model will then be incorporated into a distributed-parameter dynamic heat exchanger model integrated with a detailed frost growth model, allowing for the analysis of seasonal energy performance of ASHPs. Applying the proposed model and the experimentally validated components models in Qiao *et al*. (2015a and 2015b), the system model of the FTVI heat pump will be constructed and used to explore the dynamic characteristics during the

frosting/defrosting cycle. A detailed description of the resulting physical processes will be provided.

The remainder of this article is organized into as follows. Section 2 introduces the studied FTVI system. Section 3 presents a five-stage hot gas defrost model, along with the numerical treatments. The model of a check valve is also introduced in this section since it is used to change the direction of refrigerant flow during the RCD. Section 4 illustrates the construction of the system model of the FTVI heat pump. The simulated system dynamics during the RCD are described in Section 5. Discussions about the underlying model assumptions are given in Section 6. Model Conclusions from this work are then summarized in Section 7.

2 FTVI System Description

The studied FTVI heat pump system has been described in Qiao *et al*. (2017), and will be briefly introduced here for completeness.

Fig. 1 shows the schematic of the FTVI heat pump system, utilizing R-410A as the working fluid. The heat pump system can be operated in both cooling and heating mode. In cooling mode, refrigerant is discharged from the compressor and enters the outdoor unit for condensing. After being throttled through the upper-stage expansion valve (2), the refrigerant enters the flash tank; the vapor refrigerant is injected into the compressor, whereas the liquid refrigerant enters the lower-stage expansion valve (4), and circulates through the indoor unit. After evaporating from the indoor unit, the refrigerant then enters the suction port of the compressor to complete the closed-loop cycle. In heating mode, the electrical coil of the four way valve is energized, and therefore the refrigerant flow direction is reversed. The refrigerant exiting the compressor circulates through the indoor unit for condensing, then expands through the upper-stage expansion valve (2), and enters the flash tank. The vapor refrigerant is injected into the compressor;

meanwhile the liquid refrigerant circulates through the lower-stage expansion valve (3), evaporates in the outdoor coil, and then enters the compressor to complete the cycle.

The system can be operated either with or without vapor injection by controlling an injection control valve (1) located in the vapor injection line. The vapor injection control valve is close to the compressor to minimize the re-expansion of compressed vapor trapped between the control valve and the injection port of the compressor. The upper-stage expansion valve utilized in the system is an electronic expansion valve (EEV) controlled by an electric stepper motor, and the lower-stage expansion valve is a thermostatic expansion valve (TXV). A small, belt-shaped electric heater is wrapped around the tube surface of the vapor injection line in order to introduce a certain degree of superheat to the injected vapor.

3 Model Development

The construction of a complete cycle model for the studied FTVI heat pump system requires component submodels for the heat exchangers, vapor injection scroll compressor, flash tank, check valve, reversing valve, EEV, TXV and pipes. For the sake of brevity, this paper will only describe the check valve model and the hot-gas defrost model, which have not been presented in our previous work. The models for refrigerant flow, frost, and other components can be found in Qiao *et al*. (2015a and 2017).

3.1 Check Valve Model

The check valve allows fluid to flow through in only one direction. It is commonly used in heat pump systems to regulate the direction of the refrigerant flow when switching between the heating and cooling modes.

The on/off state of the check valve can be determined by

$$\frac{d\varphi}{dt}=\begin{cases}\dfrac{\varphi_{\max}-\varphi}{\tau} & \text{if } \Delta p>\Delta p_{open}\\ \dfrac{\varphi_{\min}-\varphi}{\tau} & \text{otherwise}\end{cases} \tag{1}$$

where φ is the current valve opening. $\varphi_{\max}$ is the maximum opening of the valve, i.e., 100%. $\varphi_{\min}$ is the minimum opening of the valve, i.e., 0.01%. τ is the time constant.

The mass flow rate through the valve can be calculated as

$$\dot{m}=\varphi\frac{\sqrt{\rho_{in}\Delta p}}{f} \tag{2}$$

where ρ_{in} is the inlet refrigerant density, Δp is the pressure drop across the valve, and f is the friction factor.

3.2 Hot-gas Defrost Model

Developing a detailed, physics-based hot gas defrost model is not possible given the fact that hot gas defrost is an extremely complex phenomenon involving simultaneous heat and mass transfer mechanisms: condensation of high pressure and high temperature refrigerant gas; heat conduction through tubes and fins; sensible heat transfer of the frost layer; melting and sublimation of the frost layer; vaporization of retained melted water. Meanwhile, the stochastic nature of the defrosting process substantially increases modeling complexity. Therefore, the defrosting process must be idealized in order to obtain a practical model. In this study, the defrosting process is subdivided into five stages: preheating, melting start, melting, vaporizing, and dry heating. Unlike the model in Dopazo *et al.* (2010) which separates analysis for tubes and fins, the proposed model unifies the analyses to maintain the consistency with our frost growth model in Qiao *et al.* (2017). The temperature profile of each stage is shown in Fig. 2 to 6. In these figures, the red dots represent the center of an element, whereas the blue dots represent the interface between adjacent elements.

This proposed defrost model is incorporated into a distributed-parameter dynamic heat exchanger model integrated with a detailed frost growth model proposed in Qiao *et al*. (2017) to allow for the prediction of the dynamic performance of ASHPs during the frosting/defrosting cycle.

3.2.1 Preheating Stage

In this stage, the high pressure and high temperature refrigerant gas will heat up the wall. This stage comes to an end once the temperature at the interface between the wall and the frost reaches the melting point of ice, i.e., 273.15 K. The heat flow is transferred from the refrigerant to the internal surfaces of the wall by convection, then to the external surfaces of the wall and the frost layer by conduction, and finally dissipated into the ambient either by natural (fan is Off) or forced convection (fan is On). Frost might sublimate during the process. In this stage, there is no phase change, and the energy storage of the wall and the frost layer increases. Meanwhile, there is no energy storage at the interface, and all the energy congregates at the center. The rate of temperature change with time at the center depends on the net rate of incoming heat flow from the adjacent interfaces. The constituent equations of this stage are Eq. (3) - (9).

$$\alpha_r \left(T_r - T_{w,i}\right) = k_w \frac{T_{w,i} - T_w}{\delta_w / 2} \tag{3}$$

$$\rho_w c_{p,w} \delta_w \frac{dT_w}{dt} = k_w \frac{T_{w,i} + T_{w,o} - 2T_w}{\delta_w / 2} \tag{4}$$

$$k_w \frac{T_w - T_{w,o}}{\delta_w / 2} = k_f \frac{T_{w,o} - T_f}{\delta_f / 2} \tag{5}$$

$$\rho_f c_{p,f} \delta_f \frac{dT_f}{dt} = k_f \frac{T_{w,o} + T_{fs} - 2T_f}{\delta_f / 2} \tag{6}$$

$$\frac{d\delta_f}{dt} = 0 \tag{7}$$

When the fan is On during the defrosting process, the heat transport between the frost surface and the air stream is determined by

$$k_f A_o \frac{T_f - T_{fs}}{\delta_f / 2} = \dot{m}_a c_{p,a} \left(T_{fs} - T_{a,in} \right) \left[1 - \exp\left(- \frac{\alpha_a A_{o,eff}}{\dot{m}_a c_{p,a}} \right) \right] + \dot{m}_a \left(\omega_{fs} - \omega_{a,in} \right) \left[1 - \exp\left(\frac{\alpha_a A_{o,eff}}{\dot{m}_a c_{p,a} Le^{2/3}} \right) \right] \Delta h_{ig} \tag{8}$$

When the fan is Off during the defrosting process, the heat from the frost layer into the ambient is dissipated by natural convection.

$$k_f A_o \frac{T_f - T_{fs}}{\delta_f / 2} = A_{o,eff} \left[\alpha_a \left(T_{fs} - T_{amb} \right) + \frac{\alpha_a}{c_{p,a} Le^{2/3}} \left(\omega_{fs} - \omega_{amb} \right) \Delta h_{ig} \right] \tag{9}$$

3.2.2 Melting Start Stage

Once the temperature at the interface between the wall and the frost reaches the melting point of ice, the frost adhering to the wall starts to thaw. As a result, a water film appears on the wall. As the frost continues to melt, the thickness of the water film increases until it reaches the maximum thickness. Analytically computing the maximum surface water on the coil after defrosting is challenging because it is determined by many factors. These factors include the gravity effect, water viscosity, coil geometry (tube pitch, row pitch, fin type, fin density, and tube diameter), surface energy of the materials, and coil orientation (horizontal, vertical, or tilted), etc. The maximum surface water per unit of surface area held on the coil is approximately 0.050 kg/m2 (Krakow *et al.*, 1992b). During this stage, the temperature at the interface between the water film and the frost layer remains at 273.15 K. The constituent equations of this stage are Eq.(3), (4), (8) or (9), (10) - (14).

$$k_w \frac{T_w - T_{w,o}}{\delta_w / 2} = k_{H_2O} \frac{T_{w,o} - T_{H_2O}}{\delta_{H_2O} / 2} \tag{10}$$

$$\rho_{H_2O} c_{p,H_2O} \delta_{H_2O} \frac{dT_{H_2O}}{dt} = k_{H_2O} \frac{T_{w,o} + 273.15 - 2T_{H_2O}}{\delta_{H_2O} / 2} \tag{11}$$

$$-\rho_f \Delta h_{if} \frac{d\delta_f}{dt} = k_{H_2O} \frac{T_{H_2O} - 273.15}{\delta_{H_2O} / 2} + k_f \frac{T_f - 273.15}{\delta_f / 2} \tag{12}$$

$$\rho_f c_{p,f} \delta_f \frac{dT_f}{dt} = k_f \frac{273.15 + T_{fs} - 2T_f}{\delta_f / 2} \tag{13}$$

$$\frac{d\delta_{H_2O}}{dt} = -\frac{d\delta_f}{dt} \tag{14}$$

3.2.3 Melting Stage

In this stage, the frost will continue to thaw, and the melted frost will drain from the coil surfaces. As a consequence, a gap forms between the water film and the frost layer. The volume formerly filled by the melted frost is replaced by the surrounding air. Through this air gap, heat is transferred by conduction. As the melting process proceeds, the air gap increases and the heat supply will decrease. During this stage, the thickness of the water film remains constant at its maximum thickness. The temperature at the interface between the air gap and the frost layer remains at 273.15 K. This stage ends when the frost layer has melted completely. The mathematical representation of the melting completion is that the thickness of the frost layer is less than 10^{-3} mm. The constituent equations of this stage are Eq.(3), (4), (8) or (9), (10), (13), (15) - (19).

$$\rho_{H_2O} c_{p,H_2O} \delta_{H_2O} \frac{dT_{H_2O}}{dt} = k_{H_2O} \frac{T_{w,o} - T_{H_2O}}{\delta_{H_2O} / 2} + \frac{T_a - T_{H_2O}}{\frac{\delta_a}{2k_a} + \frac{\delta_{H_2O}}{2k_{H_2O}}} \tag{15}$$

$$\rho_a c_{p,a} \delta_a \frac{dT_a}{dt} = \frac{T_{H_2O} - T_a}{\frac{\delta_{H_2O}}{2k_{H_2O}} + \frac{\delta_a}{2k_a}} + k_a \frac{273.15 - T_a}{\delta_a / 2} \tag{16}$$

$$-\rho_f \Delta h_{if} \frac{d\delta_f}{dt} = k_a \frac{T_a - 273.15}{\delta_a / 2} + k_f \frac{T_f - 273.15}{\delta_f / 2} \tag{17}$$

$$\frac{d\delta_a}{dt} = -\frac{d\delta_f}{dt} \tag{18}$$

$$\frac{d\delta_{H_2O}}{dt} = 0 \tag{19}$$

3.2.4 Vaporizing Stage

In this stage, only melted water remains on the coil surfaces. This stage ends when the retained water completely vaporizes, meaning the thickness of the water film is less than 10^{-3} mm. The constituent equations of this stage are Eq.(3), (4), (10), (20) - (22).

$$\rho_{H_2O} c_{p,H_2O} \delta_{H_2O} \frac{dT_{H_2O}}{dt} = k_{H_2O} \frac{T_{w,o} + T_{H_2O,s} - 2T_{H_2O}}{\delta_{H_2O} / 2} \tag{20}$$

The vaporization rate of the surface water is assumed to be proportional to the difference between the saturation density of water vapor at $T_{\mathrm{H2O,s}}$ and the density of water vapor in the ambient air. $T_{\mathrm{H2O,s}}$ is the surface temperature of the retained water. The vaporization coefficient of the surface water c_{sv} is estimated to be 0.0085 m/s (Krakow *et al.*, 1992b).

$$\rho_{H_2O} \frac{d\delta_{H_2O}}{dt} = c_{sv} \left(\rho_{H_2O,amb} - \rho_{H_2O,s} \right) \tag{21}$$

$$k_{H_2O} \frac{T_{H_2O} - T_{H_2O,s}}{\delta_{H_2O} / 2} = \alpha_a \left(T_{H_2O,s} - T_{amb} \right) + c_{sv} \left(\rho_{H_2O,s} - \rho_{H_2O,amb} \right) \Delta h_{fg} \tag{22}$$

3.2.5 Dry Heating Stage

In this stage, there is only sensible heat transfer between the wall and the ambient since there is no water retention on the coil surfaces. Once this stage is reached, the defrosting process is complete. The constituent equations of this stage are Eq.(3), (4) and (23). The heat transport between the wall and the ambient is determined based on whether the fan is On or Off.

$$k_w A_o \frac{T_w - T_{w,o}}{\delta_w / 2} = \begin{cases} \dot{m}_a c_{p,a} \left(T_{w,o} - T_{a,in}\right) \left[1 - \exp\left(-\frac{\alpha_a A_{o,eff}}{\dot{m}_a c_{p,a}}\right)\right] & Fan\ On \\ \alpha_a A_{o,eff} \left(T_{w,o} - T_{amb}\right) + \varepsilon\sigma A_{face} \left(T_{w,o}^4 - T_{amb}^4\right) & Fan\ Off \end{cases} \tag{23}$$

3.2.6 Numerical Treatments

Given the discontinuous transitions between different defrosting stages in the model, special attention must be paid to avoid numerical failures during the simulation. For instance, comparing the right-sided halves of Eq. (12) and (17) indicates that the rate of frost melting changes abruptly when defrosting transitions from the second stage to the third stage. This abrupt transition imposes great difficulties for numerical integration, and special treatments are needed to smooth out the discontinuity. In order to better explain how the proposed approach works, the transition between Eq. (12) and (17) will be used as an example. Without considering other stages, the rate of frost melting can be calculated as

$$\frac{d\delta_f}{dt} = y \cdot \left.\frac{d\delta_f}{dt}\right|_{2nd} + (1 - y) \cdot \left.\frac{d\delta_f}{dt}\right|_{3rd} \tag{24}$$

where $\left.\frac{d\delta_f}{dt}\right|_{2nd}$ and $\left.\frac{d\delta_f}{dt}\right|_{3rd}$ are the rate of frost melting during the 2nd and 3rd stage, respectively.

$$y=\begin{cases} 0, \text{if } \dfrac{\delta_{H_2O}-\delta_{H_2O,\max}}{0.01\delta_{H_2O,\max}} \in [1-10^{-10},+\infty] \\ 1, \text{if } \dfrac{\delta_{H_2O}-\delta_{H_2O,\max}}{0.01\delta_{H_2O,\max}} \in (-\infty,10^{-10}-1] \\ \dfrac{1}{2}\left[\tanh\left(\tan\left(\dfrac{\delta_{H_2O}-\delta_{H_2O,\max}}{0.01\delta_{H_2O,\max}}\dfrac{\pi}{2}\right)\right)+1\right], \text{otherwise} \end{cases} \tag{25}$$

Eq. (25) indicates that when the water film thickness is less than 99% of the maximum water film thickness, the rate of frost melting is equal to the rate during the 2nd stage computed by Eq. (12). When the water film thickness is greater than 101% of the maximum water film thickness, the rate of frost melting is equal to that during the 3rd stage computed by Eq. (17). When the water film thickness is between the aforementioned rates, a differentiable function dependent upon the current water film thickness is used to interpolate smoothly between $\left.\frac{d\delta_f}{dt}\right|_{2nd}$ and $\left.\frac{d\delta_f}{dt}\right|_{3rd}$. Thus, an automatic yet smooth transition is guaranteed and the handling of "if-then-else" conditional expressions is not required. This approach can be applied to other equations, eliminating all the discontinuities and resulting in a significant improvement in numerical stability.

4 System Model

The system model shown in Fig. 7 is constructed by combining all the component models (including other experimentally validated component models presented in Qiao *et al*. (2015a, 2015b). Among these component models, special attention needs to be paid to the reversing valve model. With the reversing valve model in Qiao *et al*. (2015a), the same system model can be utilized to simulate both cooling and heating mode, and therefore no separate models are required for the individual modes, which aides modeling the system transients during the RCD.

The basic elements used to model the refrigerant flow are the control volume and the throttle. Each component model is comprised of an alternative sequence of control volumes and throttles, and always begins with a control volume and ends with a throttle (Tummescheit, 2002). Mass and energy conservation is evaluated within the control volume, whereas the momentum conservation is solved within the throttle.

The inputs to the control volume are defined as the mass flow rate and the enthalpy flow rate entering and exiting the control volume, and the outputs are the time-varying pressure and enthalpy of the control volume. The inputs to the throttle are the pressure and enthalpy of the adjacent control volumes connected to the throttle, and the outputs are the mass flow rate and enthalpy flow rate across the throttle. Thus, the outputs of the throttle are the inputs to the adjacent control volumes, whereas the outputs of the control volume are the inputs to the adjacent throttles. Therefore, each component model has the same boundary conditions: the upstream connected mass flow rate and enthalpy flow rate, and the downstream connected pressure and enthalpy (note: the downstream connected enthalpy is only used when reverse flow occurs). The modular nature of the component models allows for flexibility in the system configuration. As a result, the component models can be seamlessly linked together in an arbitrary manner, regardless of whether they are the flow equipment, like the compressors and valves, or the heat transfer equipment, like the heat exchangers.

The models are implemented using the Modelica modeling language and the Dymola 7.4 (AB Dassault Systemes, 2014) simulation environment. All the refrigerant properties are evaluated using in-house curve-fitted property routines, developed based on the REFPROP 9.0 database (Lemmon *et al*., 2010). Empirical correlations are used to calculate the heat transfer coefficients and the pressure drops on both the refrigerant side and the air side (Qiao *et al*., 2015a).

5 Simulation Results

The proposed models were applied to explore the transient characteristics of the FTVI heat pump system during the RCD. The operating condition is used in the simulation, given in Table 1. The simulation procedure is set up as follows.

In order to avoid any undesirable complications caused by the controller, the upper-stage EEV opening is fixed at 16% in heating mode. Meanwhile, the shut-off valve prior to the injection port of the compressor is opened to enable vapor injection. From Qiao *et al.* (2017), we know that the FTVI system starts to show signs of operating instability after operating in heating mode for about 50 minutes, suggesting that the defrosting needs to be initiated at that time. Therefore, the frosting cycle is terminated at 3000 sec. The RCD is initiated by energizing the reversing valve and turning off the outdoor fan, but keeping the indoor fan on. In the meantime, two three-way valves are energized to ensure that the inlet and outlet of the flash tank are not switched in the reversed mode. During the RCD, the upper-stage EEV is fully opened, and the vapor injection is disabled by closing the shut-off valve prior to the injection port of the compressor.

The defrosting process lasts for 600 sec, and is terminated at 3600 sec. The system resumes to heating mode by switching the reversing valve and turning on the outdoor fan. Meanwhile, two three-way valves are de-energized to ensure that the inlet and outlet of the flash tank are not switched. Moreover, the opening of the upper-stage EEV is switched from 100% back to 16%, and the shut-off valve prior to the injection port of the compressor opens again to enable vapor injection. Therefore, the simulation, which stops at 6000 sec, allows for a full examination of the system dynamics not only during the RCD, but also during the mode switch between frosting and defrosting.

The frosting dynamics of the FTVI system have been discussed in great detail in Qiao *et al.* (2017), and will not be repeated for brevity. The system dynamics during the RCD will be the primary focus of this paper.

When the system is reversed, the refrigerant inlets of the coils are turned into the outlets, and the refrigerant outlets of the coils are turned into the inlets. To avoid confusion, however, in this section (including figures) the inlets and outlets of the coils always follow the definitions in heating mode.

5.1 RCD Transients

A rapid refrigerant pressure equalization process occurs after defrosting is initiated. From 3000 sec to 3002 sec, the discharge pressure plummets from 2184 kPa to 1347 kPa, whereas the suction and the flash tank pressures surge from 565 kPa and 1041 kPa to 1359 kPa and 1346 kPa, respectively (Fig. 8a). The abrupt drop in the discharge pressure is due to the connection of the compressor discharge to the low pressure side, i.e., the outdoor coil. The abrupt rise of the suction pressure is due to the connection of the compressor suction to the high pressure side, i.e., the indoor coil. The rapid increase in the flash tank pressure is due to the connection of the flash tank's outlet to the indoor coil as a result of the engagement of the two three-way valves.

After the pressure equalization, the suction pressure will continue rising to 1442 kPa at 3010 sec because the previous sudden decline in the indoor coil pressures causes the stored liquid refrigerant to boil and flow towards the compressor suction. Afterwards, the suction pressure approaches the indoor coil pressures, follows their variations, and starts to decrease. From 3000 sec to 3021 sec, the indoor coil will not receive any refrigerant replenishment. During the period, the indoor coil pressures, although decreasing, are still higher than the flash tank pressure, resulting in an outgoing refrigerant flow to the flash tank. At the other end of the indoor coil, the refrigerant

is continuously drawn to the compressor. As a result, the indoor coil only contains the low pressure vapor from 3024 sec to 3030 sec. After 3021 sec, a reversed pressure difference between the indoor coil and the flash tank is established, resulting in a refrigerant flow from the flash tank to the indoor coil. However, this replenishment is insufficient to compensate the outgoing flow to the compressor. Therefore, the indoor coil is temporarily starved of refrigerant, and its pressures continue declining until reaching a minimum of 473 kPa at 3035 sec. With more refrigerant replenishment from the flash tank, the indoor coil pressures start to rise thereafter and reach a local maximum of 564 kPa at 3054 sec. However, refrigerant flow rate from the flash tank to the indoor coil reduces simultaneously due to the decline in the pressure difference between them, resulting in a subsequent dip in the indoor coil pressures. Beginning at 3081 sec, the indoor coil pressures will follow the variations in the discharge and flash tank pressures before plateauing around 730 kPa at 3300 sec (Fig. 8b). After 3300 sec, the suction and indoor coil pressure exhibit little changes until the end of the RCD.

The discharge pressure will decrease further to 1001 kPa at 3008 sec after the pressure equalization due to the previous sudden rise in the outdoor coil pressures. This results in massive condensation of refrigerant (the outdoor coil is covered by frost and its surface temperatures are low). The outdoor coil will not have any outgoing flow until 3024 sec, resulting in a rapid pressure buildup during the period. From 3000 sec to 3024 sec, the flash tank pressure is higher than the pressure at the inlet of the outdoor coil, resulting in refrigerant flowing from the flash tank to the outdoor coil. At the same time, the compressor continuously pumps refrigerant into the outdoor coil at the other end. Therefore, the discharge pressure (also close to the pressure at the outlet of the outdoor coil) rises to a maximum of 1362 kPa at 3024 sec. Afterwards, the reversed pressure difference between the outdoor coil and the flash tank causes the refrigerant to flow from the

outdoor coil to the flash tank, leading to a drop in the discharge and outdoor coil pressures. At 3088 sec, the discharge pressure reaches a minimum of 1064 kPa, and stabilizes until 3120 sec. With the progression of frost melting, a portion of the outdoor coil is exposed to the ambient air, resulting in an increase in the coil surface temperatures. This leads to a rise in the discharge pressure, which reaches 1190 kPa at 3300 sec and gradually increases to 1241 kPa at the end of RCD (Fig. 8b).

Shortly after pressure equalization, the flash tank pressure dips at 3003 sec, then reaches a maximum of 1403 kPa at 3007 sec. The incoming flow from the indoor coil is not sufficient to compensate the outgoing flow to the outdoor coil, leading to a subsequent decline in the flash tank pressure, which reaches a minimum of 874 kPa at 3110 sec. There is little restriction for refrigerant flow between the outdoor coil and the flash tank in heating mode because the upper-stage EEV is fully opened and the TXV 3 is bypassed by the check valve. Thus, the flash tank pressure will follow the variations in the outdoor coil pressures thereafter, and reach 1037 kPa at the end of the RCD (Fig. 8b).

After the initiation of defrosting, the air side heat load of the indoor coil decreases rapidly from 8.2 kW to -5.8 kW within 60 sec due to massive evaporation of the refrigerant inside the indoor coil, and continues decreasing and levels off at around -10.1 kW after 3250 sec (Fig. 9). A positive value for the air load means that the air is heated up by gaining thermal energy from the refrigerant, while a negative value means that the air is cooled by losing thermal energy to the refrigerant. During this period, the air side heat load of the outdoor coil, which largely follows the variations in the outdoor coil pressures, increases quickly first then reaches a local maximum of 8.4 kW at 3027 sec due to massive condensation of the refrigerant inside the outdoor coil. After reaching the maximum, it decreases to 4.9 kW at 3081 sec and stabilizes until 3120 sec. With the progression

of frost melting, the air side heat load of the outdoor coil rises to 10.4 kW at 3300 sec, and exhibits little change thereafter. Meanwhile, the compressor power decreases from 2.4 kW to 0.6 kW after the pressure equalization due to the lower compressor pressure ratio. Starting from 3022 sec, the compressor power starts to increase, and reaches a local maximum of 1.2 kW at 3036 sec. This is a result of the augmented compressor pressure ratio, and then declines to around 0.8 kW at 3200 sec. Afterwards, the compressor power will increase gradually to 0.9 kW at the end of the RCD due to the gradual elevation in the discharge pressure during the period.

The refrigerant superheat leaving the indoor coil declines to zero for 20 sec after defrost initiation, indicating that two-phase refrigerant flashes towards the compressor (Fig. 10). Then the superheat increases rapidly before reaching a maximum of 33 K at 3035 sec when the indoor coil pressure reaches a minimum. The superheat decreases subsequently when the indoor coil pressures rise. At 3328 sec, the indoor coil superheat starts to decrease at 9 K, and finally reaches 7.5 K at the end of RCD. Thus, the TXV 4 should be open during the period. The subcooling leaving the outdoor coil does not appear until 3025 sec, and shows little changes since then. This indicates that the temperature of liquid refrigerant leaving the outdoor coil varies insignificantly during frost melting (Fig. 10).

The refrigerant mass distribution in various components is shown in Fig. 11. After the defrosting initiation, the refrigerant in the indoor coil depletes rapidly due to the quick outgoing flows to the outdoor coil and flash tank. During the defrosting cycle, refrigerant mass in the indoor coil only accounts for about 5% of the total charge, compared to about 50% of the total charge during the frosting cycle. During this period, the refrigerant in the outdoor coil increases significantly because of the replenishment from the flash tank and indoor coil. At 3026 sec, the refrigerant mass in the outdoor coil reaches the peak, accounting for approximately 70% of the

total charge. With the progression of the defrosting cycle, however, the excess refrigerant stored in the outdoor coil will redistribute to the flash tank and pipes. Eventually, 30% of the total charge resides in the outdoor coil, 25% in the flash tank, and 40% in the compressor and connecting pipes. Meanwhile, the liquid level in the flash tank increases rapidly after defrosting initiation because a large amount of the refrigerant flushes towards the flash tank from the indoor coil. Since it acts as a receiver during the defrosting, the flash tank will ultimately be filled with liquid refrigerant.

The variations in the refrigerant mass flow rates are shown in Fig. 12. The positive mass flow denotes the incoming flow, whereas the negative flow denotes the outgoing flow. Right after the engagement of the reversing valve and three-way valves, reverse flows occur at the inlet of the indoor coil, the outlet of the outdoor coil, and the inlet and outlet of the flash tank. From 3023 sec to 3027 sec, reverse flows occur at the outlet of the indoor coil, the inlet of the outdoor coil, and the inlet and outlet of the flash tank due to the reverse pressure differences. The transients of refrigerant mass flow rates nearly dissipate after 3150 sec.

The time evolution of the frost thickness on each tube during the RCD is given in Fig. 13. The frost starts to melt soon after the initiation of defrosting, and the outdoor coil is cleared of frost before 3400 sec. Once the frost has melted, the retained melted water will vaporize from the coil surface. By the defrost termination, a portion of the outdoor coil is dry and directly exposed to the ambient air, resulting in a gradual increase in the discharge and outdoor coil pressures.

5.2 Restoration Transients

At 3600 sec, the defrosting process is terminated and the system resumes to heating mode. Likewise, fast pressure transients occur as the reversing valve is switched. The discharge pressure plummets to 889 kPa, then increases to 1552 kPa within 20 seconds. During the same period, the suction pressure climbs to 989 kPa before declining to 727 kPa, while the flash tank pressure rises

to 1098 kPa, then declines to 988 kPa (Fig. 8c). The compressor power decreases sharply to 0.4 kW at the defrosting termination due to dramatic changes in the compressor pressure ratios, and increases thereafter (Fig. 9). Unlike the beginning of the defrosting process where the indoor coil is starved of refrigerant due to the delayed refrigerant replenishment from the flash tank through the TXV 4, the pressure transients during the restoration process are less dramatic because of the earlier refrigerant supply to the outdoor coil from the flash tank (reverse flow occurs at the inlet of the outdoor coil at 3603 sec, as shown in Fig. 12b). On the other hand, the pressure differences between the indoor and outdoor coils are much smaller during the defrosting cycle, which is beneficial to a relatively fast pressure recovery compared to the defrost initiation.

5.3 Defrosting Efficiency

During the defrosting, the total energy supply from the refrigerant predicted by the model is 4791.9 kJ. The energy used to melt the frost is 849.8 kJ, which accounts for 17.7% of the total energy. This percentage is consistent with the study by Niederer (1976), i.e., the efficiency for a typical defrosting process was 15-25%. The breakdown of the energy flow during the defrosting cycle is shown in Table 2.

6 Discussions

Due to the stochastic nature, a series of idealization have been made to attain a pragmatic defrost model, and they are discussed as follows.

(1) The frosting model used in the study is unable to capture the refrosting characteristics of the heat exchangers. In general, the defrosting and refrosting behavior becomes periodic after the third or fourth cycle. Due to the fin geometry, the corner formed by two adjacent fins tends to hold droplets during the defrosting period. The droplets will freeze in subsequent refrosting

cycles with significant effects on pressure drop and heat transfer (Xia *et al*., 2006). However, due to the complex underlying physics, detailed modeling of water retention on the tube walls and fins is extremely challenging. To simplify the analysis, the frosting model assumes that all retained water has completely vaporized during the preceding defrosting cycle. With the current framework, therefore there will be no discrepancies in the results between the first and subsequent frosting/defrosting cycles if the operating conditions remain the same.

(2) Compared with the melting rate, the sublimation rate of frost is extremely small, with an average of about 1.3×10^{-5} kg/(m^2·s) in the presented study. However, this small amount of sublimation can result in latent heat flux of 37 W/m^2 (this is comparable to the sensible heat flux by natural convection) because of the large magnitude of sublimation heat of ice, i.e., 2838 kJ/kg. As a result, the latent heat transfer due to sublimation of frost must be taken into account in Eq. (7) and (8). On the other hand, mass transfer between the frost and ambient air due to sublimation yields negligible influence on the frost thickness due to its small magnitude. The shrinkage of frost is primarily caused by melting rather than sublimation. To simplify the computation, the effect of sublimation on frost thickness is neglected in Eq. (7), (12) and (17) . Otherwise, Eq. (7) becomes

$$\frac{d\delta_f}{dt}=\begin{cases}-\dfrac{\dot{m}_a\left(\omega_{fs}-\omega_{a,in}\right)}{\rho_f A_o}\left[1-\exp\left(\dfrac{\alpha_a A_{o,eff}}{\dot{m}_a c_{p,a} Le^{2/3}}\right)\right] & \textit{Fan On}\\ -\dfrac{\alpha_a A_{o,eff}}{c_{p,a} Le^{2/3}\rho_f A_o}\left(\omega_{fs}-\omega_{amb}\right) & \textit{Fan Off}\end{cases} \tag{26}$$

And the same correction should be made to Eq. (12) and (17) as well.

(3) Depending on the assumption of whether or not the frost adheres to tube walls during defrost, there are two types of prevailing models. The models with the optimistic assumption that the

frost always attaches to tube walls during melting were presented in Aljuwayhel (2006) and Krakow *et al*. (1992a). The models with the pessimistic assumption that air gaps exist between tube walls and melting frost were given in Dopazo *et al*. (2010) and Sanders (1974). Clearly, the optimistic assumption yields a shorter defrost process, whereas the pessimistic assumption results in a prolonged one. The proposed model chose the pessimistic assumption because it can ensure that the coil surface is free of frost at the end of defrost. To account for the local drainage of melted frost, it can be assumed that the frost detaches from coil surface because of gravity when the frost thickness decreases to a small value, e.g., 5% of its original thickness.

(4) In the presented study, during the RCD the outdoor fan is prevented from turning on to accelerate the temperature rise of the outdoor coil, whereas the indoor unit still operates with the fan on. In many cases, however, the indoor fan is usually turned off during defrost because of concern about the indoor thermal comfort. A comparison of the effects of fan control strategies on defrost and indoor thermal comfort requires coupling a dynamic heat pump system model with a room model and should be an interesting research topic.

7 Conclusions

A five-stage hot-gas defrost model which unifies the analysis for tubes and fins is developed in the paper. The model has been incorporated into a distributed-parameter dynamic heat exchanger model integrated with a detailed frost growth model, allowing for a comprehensive investigation on the complex system dynamics of ASHPs during the frosting/defrosting cycle. Meanwhile, numerical treatments are proposed to smooth out the discontinuous transitions between different defrosting stages to improve numerical stability.

The presented models in this paper, along with the models developed in our previous work, are used to construct the system model of an air source FTVI heat pump. The modular nature of

all the models allows for the use of the same system model to simulate both heating and cooling mode. Dynamic simulation has been conducted to explore the transient fluid flow and heat transfer phenomena of the system during the frosting/defrosting cycle, and a detailed description of the resulting physical processes is provided. It is evident that the presented study facilitates a deep understanding of the dynamic characteristics of the FTVI heat pump during the RCD, and is beneficial to the analysis of seasonal energy performance. Moreover, the insights gained in the study can be employed to assist in the design of the defrost control strategy to improve the system performance.

ACKNOWLEDGMENTS

This work was supported by the Modeling and Optimization Consortium at the University of Maryland.

REFERENCES

AB Dassault Systemes, 2014. Dymola 7.4.

Aljuwayhel, N.F., 2006. Numerical and experimental study of the influence of frost formation and defrosting on the performance of industrial evaporator coils. Ph.D. thesis, University of Wisconsin-Madison, USA.

Anand, N.K., Schliesing, J.S., O'Neal, D.L., Peterson, K., 1989. Effects of outdoor coil fan pre-start on pressure transients during the reverse cycle defrost of a heat pump. ASHRAE Trans. 95, 699-704.

Chen, Y. and Guo, X., 2009. Dynamic defrosting characteristics of air source heat pump and effects of outdoor air parameters on defrost cycle performance. Appl. Therm. Eng. 29, 2701-2707.

Dopazo, J.A., Fernandez-Seara, J., Uhía, F.J., Diz, R., 2010. Modelling and experimental validation of the hot-gas defrost process of an air-cooled evaporator. Int. J. Refrigeration 33, 829-839.

Huang, D., He, Z., Yuan, X., 2007. Dynamic characteristics of an air-to-water heat pump under frosting/defrosting conditions. Appl. Therm. Eng. 27(11-12), 1996-2002.

Huang, D., Yuan, X., Zhang, X., 2004. Effects of fan-starting methods on the reverse-cycle defrost performance of an air to water heat pump. Int. J Refrigeration 27(8), 869-875.

Krakow, K.I., Lin, S., Yan, L., 1993. An idealized model of reversed-cycle hot gas defrosting - Part 1: Theory. ASHRAE Trans. 99, 317-327.

Krakow, K.I., Yan, L., Lin, S., 1992a. A model of hot gas defrosting of evaporators - Part 1: Heat and mass transfer theory. ASHRAE Trans. 98, 451-461.

Krakow, K.I., Yan, L., Lin, S., 1992b. A model of hot gas defrosting of evaporators - Part 2: Experimental analysis. ASHRAE Trans. 98, 462-474.

Lemmon, E.W., Huber, M.L., McLinden, M.O., 2010. NIST reference fluid thermodynamic and transport properties - REFPROP version 9.0. National Institute of Standard and Technology.

Liu, Z., Li, X., Wang, H., Peng, W., 2008. Performance comparison of air source heat pump with R407C and R22 under frosting and defrosting. Energ. Convers. Manage. 49(2), 232-239.

Liu, Z., Tang, G., Zhao, F., 2003. Dynamic simulation of air-source heat pump during hot-gas defrost. Appl. Therm. Eng. 23(6), 675-685.

Niederer, D.H., 1976. Frosting and defrosting effects on coil heat transfer. ASHRAE Trans. 82, 467-473.

O'Neal, D.L. and Peterson, K., 1990. A comparison of orifice and TXV control characteristics during the reverse-cycle defrost. ASHRAE Trans. 96, 337-343.

O'Neal, D.L., Peterson, K., Anand N.K., 1991. Effect of shot-tube orifice size on the performance of an air source heat pump during the reverse-cycle defrost. Int. J. Refrigeration 14, 52-57.

O'Neal, D.L., Peterson, K., Anand, N.K., Schliesing J.S., 1989. Refrigeration system dynamics during the reverse cycle defrost. ASHRAE Trans. 95, 689-698.

Payne, V. and O'Neal, D.L., 1995. Defrost cycle performance for an air-source heat pump with a scroll and a reciprocating compressor. Int. J. Refrigeration 18, 107-112.

Qiao, H., Aute, V., Radermacher, R., 2015a. Transient modeling of a flash tank vapor injection heat pump system - Part I: Model development. Int. J. Refrigeration 49, 169-182.

Qiao, H., Aute, V., Radermacher, R., 2017. Dynamic modeling and characteristic analysis of a two-stage vapor injection heat pump system under frosting conditions. Int. J. Refrigeration 84, 181-197.

Qiao, H., Laughman, C., Aute, V., Radermacher, R., 2016. An advanced switching moving boundary heat exchanger model with pressure drop. Int. J. Refrigeration 84, 154-171.

Qiao, H., Xu, X., Aute, V., Radermacher, R., 2015b. Transient modeling of a flash tank vapor injection heat pump system - Part II: Simulation results and experimental validation. Int. J. Refrigeration 49, 183-194.

Sanders, C.T., 1974. The influence of frost formation and defrosting on the performance of air coolers. Ph.D. thesis, Delft Technical University, Netherlands.

Tummescheit, H., 2002. Design and implementation of object-oriented model libraries using Modelica. Ph.D. thesis, Department of Automatic Control, Lund Institute of Technology, Sweden.

Wang, X., Hwang, Y., Radermacher, R., 2009. Two-stage heat pump system with vapor-injected scroll compressor using R410A as a refrigerant. Int. J. Refrigeration 32, 1442-1451.

Xia, Y., Zhong, Y., Hrnjak, P.S., Jacobi, A.M., 2006. Frost, defrost, and refrost and its impact on the air-side thermal-hydraulic performance of louvered-fin, flat-tube heat exchangers. Int. J. Refrigeration 29, 1066-1079.

List of Figure Captions

Figure 1: Schematic of the flash tank vapor injection heat pump system

Figure 2: Preheating stage

Figure 3: Melting start stage

Figure 4: Melting stage

Figure 5: Vaporizing stage

Figure 6: Dry heating stage

Figure 7: Model representation of the refrigerant side of FTVI system

Figure 8: Pressure transients: (a) - During the defrosting initiation; (b) - During the complete defrosting cycle; (c) - During the defrosting termination

Figure 9: Air side heat loads and compressor power

Figure 10: Indoor coil superheat and outdoor coil subcooling

Figure 11: Predicted refrigerant mass distribution and flash tank liquid height

Figure 12: Refrigerant mass flow rates: (a) - Defrosting initiation; (b) - Defrosting termination

Figure 13: Variations in the frost thickness of each tube

List of Table Captions

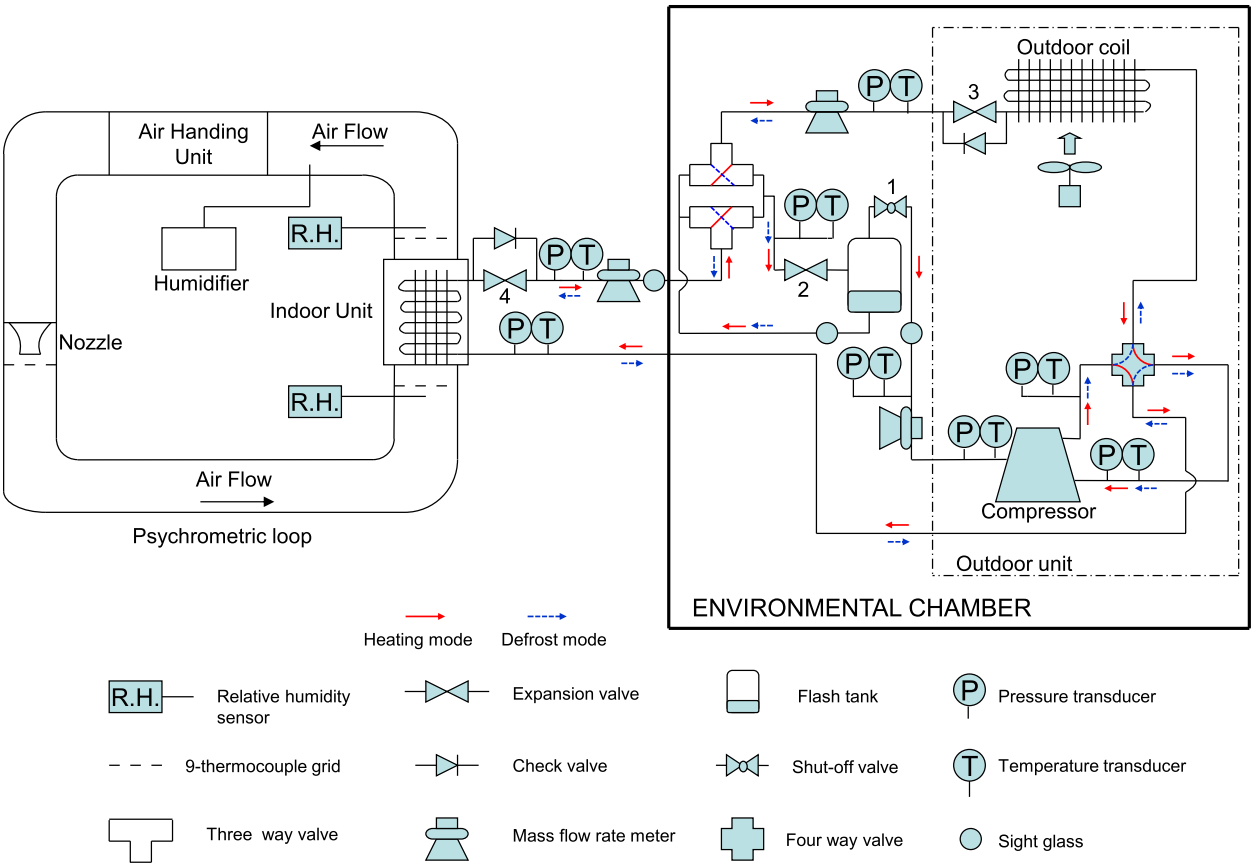

Figure 1: Schematic of the flash tank vapor injection heat pump system

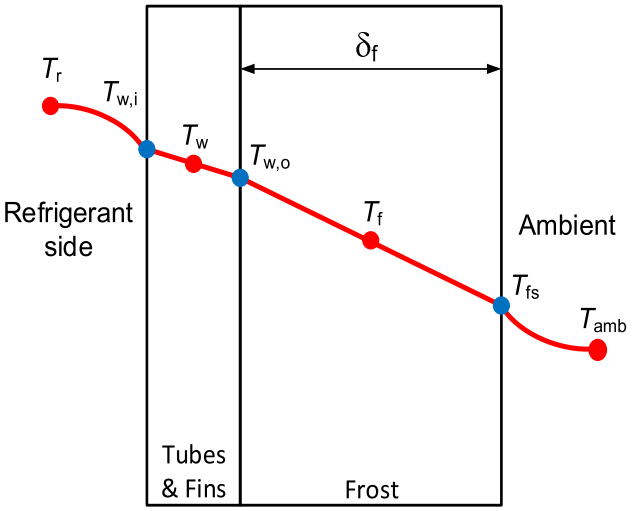

Figure 2: Preheating stage

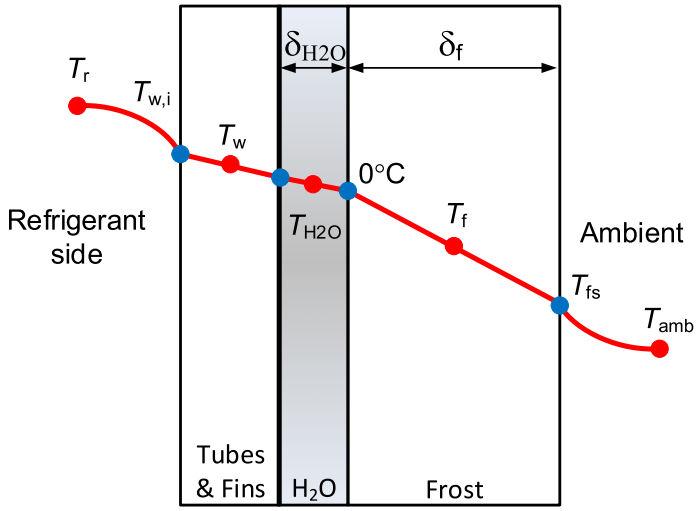

Figure 3: Melting start stage

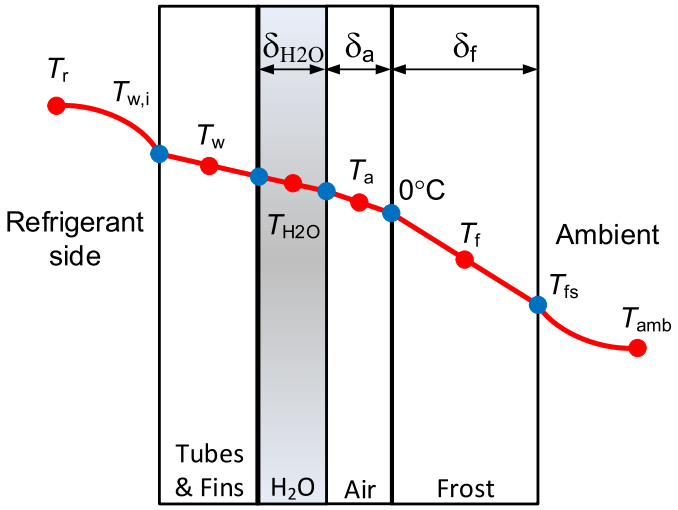

Figure 4: Melting stage

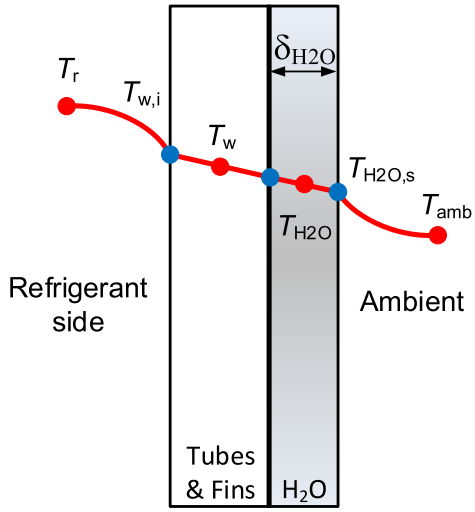

Figure 5: Vaporizing stage

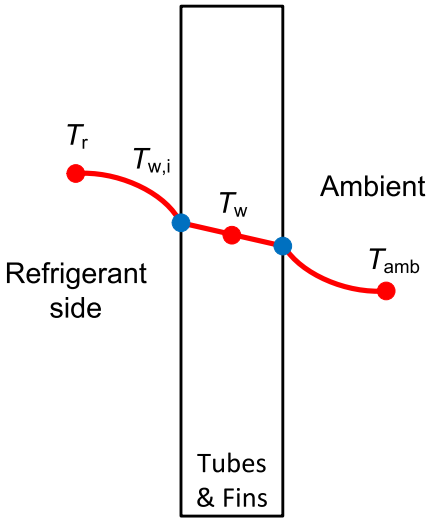

Figure 6: Dry heating stage

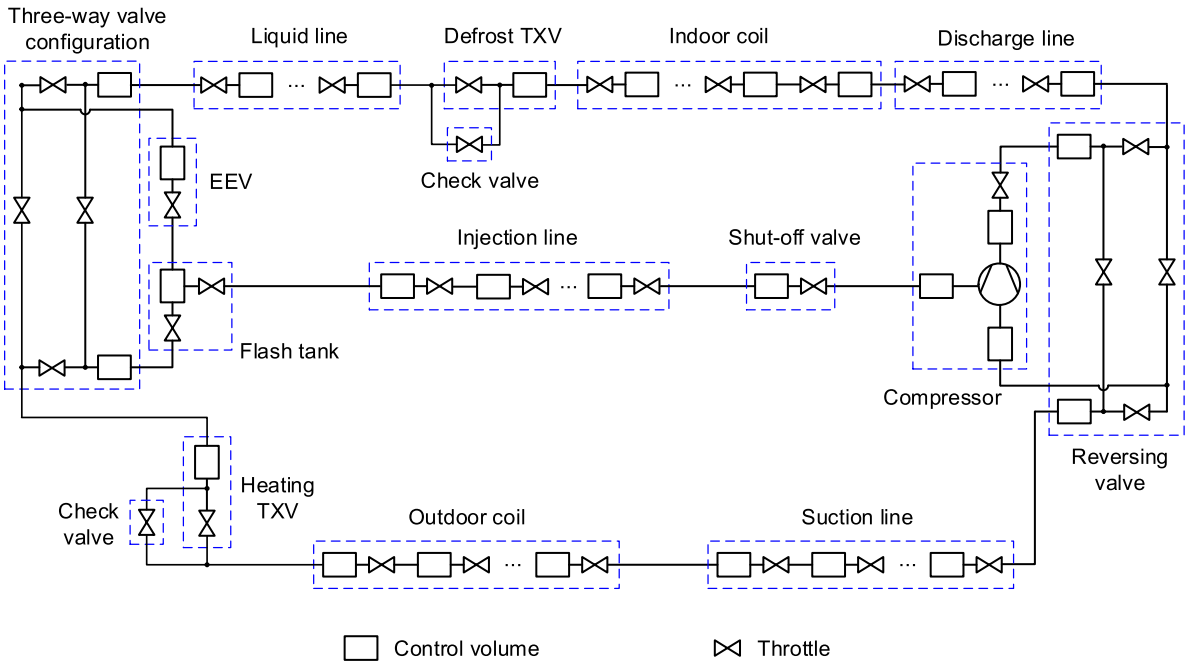

Figure 7: Model representation of the refrigerant side of FTVI system

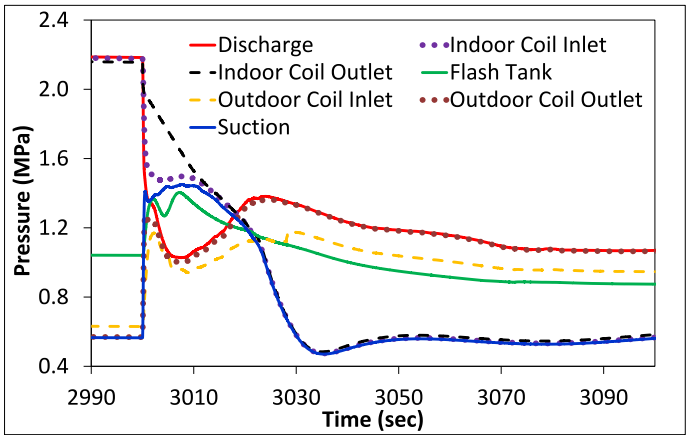

(a)

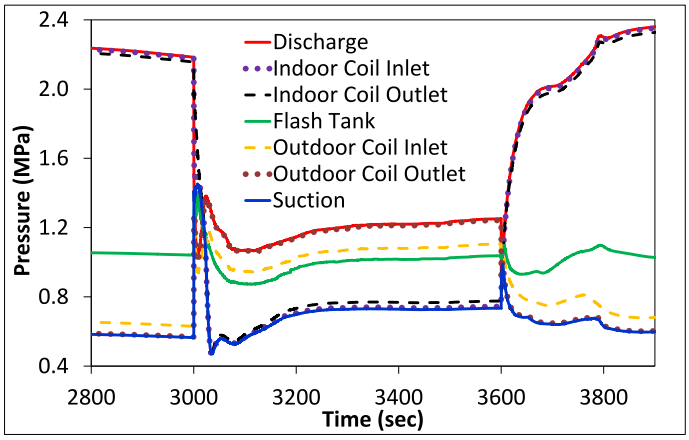

(b)

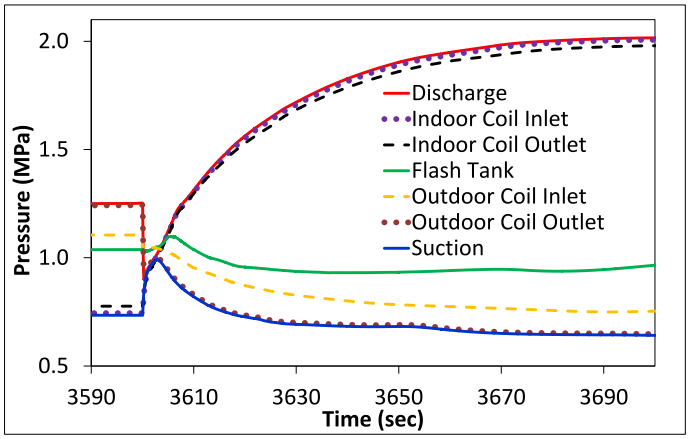

(c)

Figure 8: Pressure transients: (a) - During the defrosting initiation; (b) - During the complete defrosting cycle; (c) - During the defrosting termination

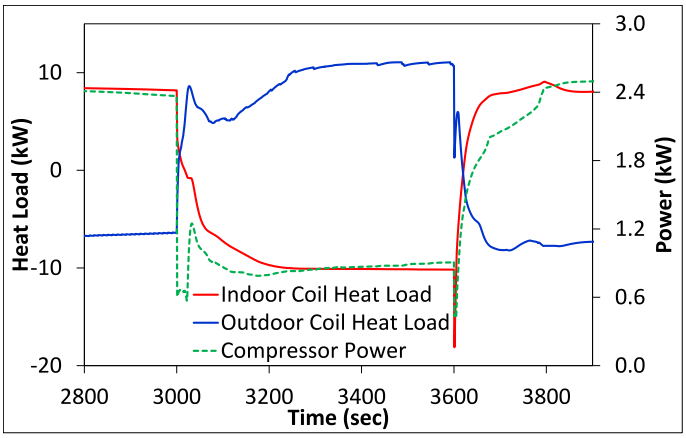

Figure 9: Air side heat loads and compressor power

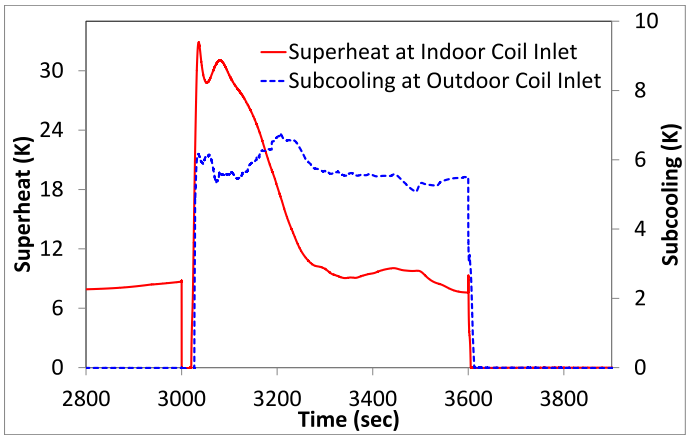

Figure 10: Indoor coil superheating and outdoor coil subcooling

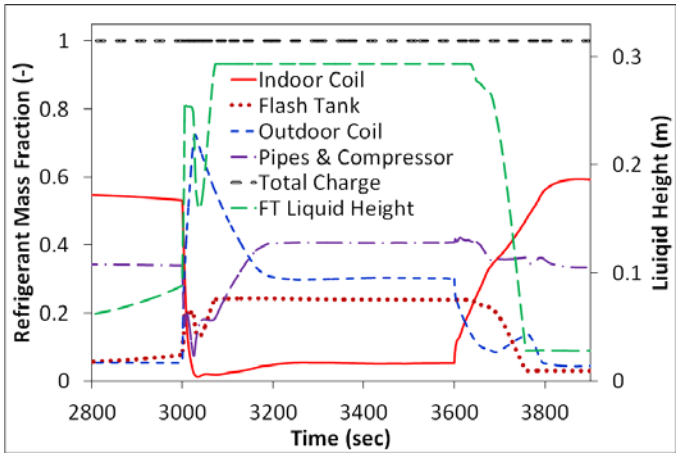

Figure 11: Predicted refrigerant mass distribution and flash tank liquid height

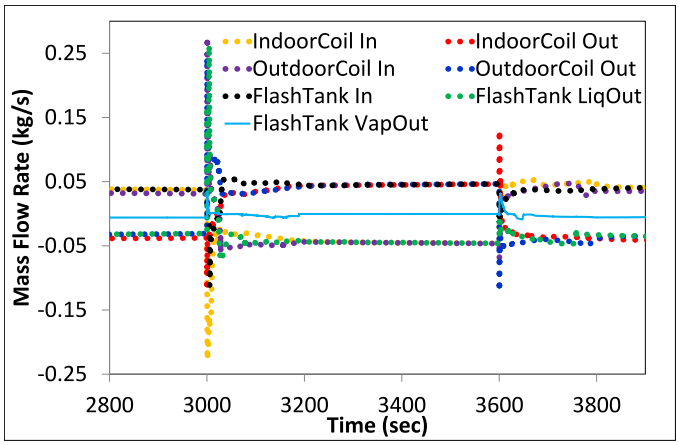

(a)

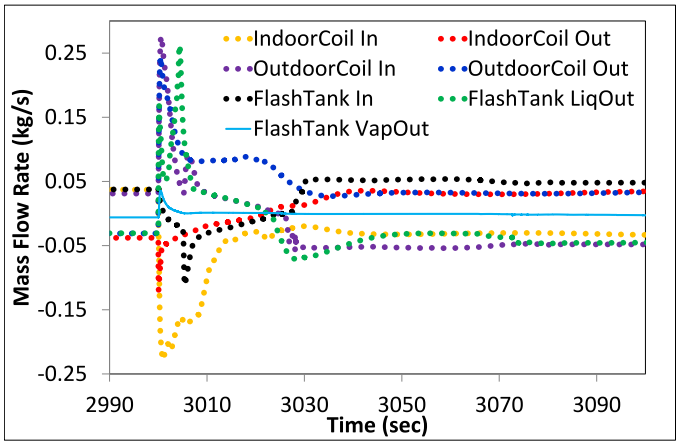

(b)

Figure 12: Refrigerant mass flow rates: (a) - Defrosting initiation; (b) - Defrosting termination

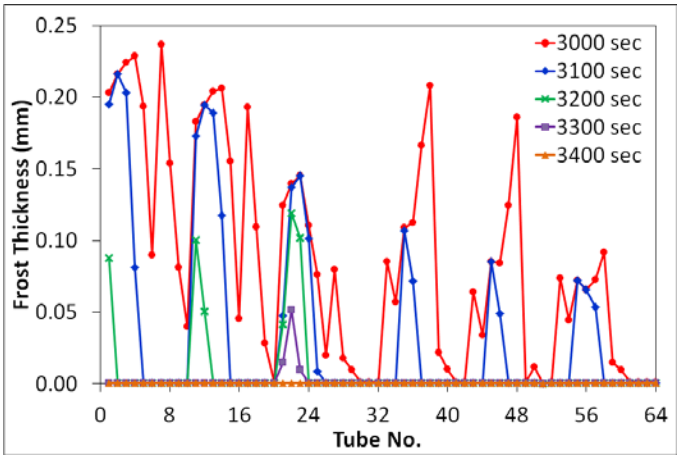

Figure 13: Variations in the frost thickness of each tube

Table 1: Operating conditions in the simulation

ASHRAE Condition	Indoor Dry Bulb [°C]	Indoor RH [-]	Outdoor Dry Bulb [°C]	Outdoor RH [-]
Frost Accumulation	21.1	48%	1.7	82%

Table 2: Energy breakdown during the RCD

Parameter	Model Prediction (kJ)	Percentage
Q_r	4791.9	100%
Q_a	3531.4	73.7%
Q_{sen}	611.1	12.8%
Q_{lat}	2920.3	60.9%
Q_{st}	410.8	8.6%
Q_{melt}	849.8	17.7%

Q_r: the total energy supplied by the refrigerant

Q_a: the total energy transferred to the ambient

Q_{sen}: the convective heat transfer to the ambient

Q_{lat}: the latent energy transferred to the ambient

Q_{st}: the energy stored by tubes and fins

Q_{melt}: the energy used to warm and melt the frost